

**Polyoxometallates@zeolitic-imidazolate-framework derived  
bimetallic tungsten-cobalt sulfide/porous carbon nanocomposites as  
efficient bifunctional electrocatalysts for hydrogen and oxygen  
evolution**

Zheng Huang <sup>a</sup>, Zhuxian Yang <sup>a</sup>, Zahid Hussain <sup>a</sup>, Binling Chen <sup>a</sup>, Quanli Jia <sup>b</sup>,  
Yanqiu Zhu <sup>a</sup>, Yongde Xia <sup>a,\*</sup>

<sup>a</sup> *College of Engineering, Mathematics and Physical Sciences, University of Exeter, Exeter EX4  
4QF, UK*

<sup>b</sup> *Hennan Key Laboratory of High Temperature Functional Ceramics, Zhengzhou University,  
Zhengzhou, 450052, China*

\* To whom correspondence should be addressed. Email: [y.xia@exeter.ac.uk](mailto:y.xia@exeter.ac.uk). Tel: +44 01392  
723683.

## Abstract

Hydrogen is one of the most promising sustainable energy among numerous new energy resources. Electrocatalytic water splitting for H<sub>2</sub> generation is a clean and sustainable approach due to the use of widely existed water as resource. The searching for efficient and low-cost non-precious metal based electrocatalysts for water splitting, including both cathodic hydrogen evolution reaction (HER) and anodic oxygen evolution reaction (OER), still remains a great challenge. In this work we report a simple method that utilizes the one-pot in-situ synthesized POMs@ZIFs (POMs= Polyoxometallates, ZIFs=Zeolitic imidazolate frameworks) as precursor for the production of WS<sub>2</sub>/Co<sub>1-x</sub>S/N, S co-doped porous carbon nanocomposite as efficient electrocatalysts. These precursors POMs@ZIFs can effectively prevent the agglomeration of metal compound particles during heat treatment and leads to homogeneous dispersion of metal active sites within carbon matrix. The resulting bimetallic Co-W sulfide/heteroatom doped porous carbon composites show significant improvement in electrocatalytic activity towards both OER (Tafel slop of 53 mV dec<sup>-1</sup> with overpotential of 0.365 V @10 mA cm<sup>-2</sup> current density in 1 M KOH media) and HER (Tafel slop of 64 mV dec<sup>-1</sup> with overpotential of 0.250 V @10 mA cm<sup>-2</sup> current density in 0.5 M H<sub>2</sub>SO<sub>4</sub> solution). This work opens up a new way to obtain low cost bifunctional electrocatalysts towards both OER and HER in water splitting.

## 1. Introduction

With the increase of the global energy demand, current energy solutions which greatly rely on non-renewable fossil fuels have become more and more unsustainable since the emitted pollutions from the combustion of fossil fuels have exerted a catastrophic influence on the global environment. To tackle these problems, much effort has been devoted to the development of new sustainable energies. Owing to the advantages of high energy density, zero emission of pollutants, non-toxicity and renewability, hydrogen (H<sub>2</sub>) has emerged to be a promising alternative energy carrier to the conventional hydrocarbon-based petrochemicals. However, hydrogen does not exist naturally and normally it has to be produced from other energy resources. Amongst numerous hydrogen generation approaches, large scale production of highly pure H<sub>2</sub> via electrochemical water splitting is the most clean and sustainable strategy, as the only raw resource used is the cheap and widely existed water.[1] In electrocatalytic water splitting process, the intermittent renewable energies, such as tidal, wind or solar energy, can be readily transferred to electrical energy, which provide driving force to promote the chemical reaction of water splitting and generate H<sub>2</sub> that can be easily stored, transport and save for later use.[2] Water can be split into H<sub>2</sub> and O<sub>2</sub> via two half reactions: the cathodic hydrogen evolution reaction (HER) that reduces water into hydrogen molecules ( $2\text{H}^+ + 2\text{e}^- \rightarrow \text{H}_2$ ) in acidic electrolyte, and the anodic oxygen evolution reaction (OER) that oxidizes water into oxygen molecules ( $4\text{OH}^- \rightarrow 4\text{e}^- + 2\text{H}_2\text{O} + \text{O}_2$ ) in alkaline electrolyte. Both reactions can be promoted by the use of efficient electrocatalysts. The benchmark electrocatalysts for both reactions contain precious metals such as Pt and Ir. However, the scarcity of these precious metals results in high cost and prohibits their large scale industrial applications. Moreover, the poor stability of these materials in the electrochemical reactions is another barrier to inhibit their wide range of

applications. Therefore, to develop cheap and efficient electrocatalysts are highly imperative for the commercial implementation of large-scale water splitting devices that can produce high purity hydrogen in the next-generation energy scenario.

In the past decades, huge efforts have been dedicated to the substitution of precious metal catalysts with cheaper transition metal based materials. The group six transition metal chalcogenides ( $\text{MX}_2$  where  $\text{M} = \text{Mo}, \text{W}$  and  $\text{X} = \text{S}, \text{Se}$ ) are one of the most exciting catalyst families,[3] and the promising electrochemical applications of these layered transition metal dichalcogenides have been comprehensively reviewed recently.[4] The atoms of these compounds are bonded together with covalent bond to form 2D layer hexagonal structures, which are stacked together via weak van der Waal's force to form 3D crystal structures. Among these transition metal dichalcogenides,  $\text{MoS}_2$  is one of the most widely studied metal chalcogenide as electrochemical water splitting catalyst, which in bulk is a semiconductor with poor performance in HER, but the nanostructured  $\text{MoS}_2$  frequently exhibits much enhanced HER performance.[5, 6] Its analogue  $\text{WS}_2$  also has a similar prospective[7] and experiences the same issues as that of  $\text{MoS}_2$  has, such as low active site density and poor electronic conductivity, which inevitably inhibit their electrocatalytic performance in HER. The active site density of the catalyst can usually be increased by the formation of nanoscale structures or dispersion of the active components in highly porous supports,[8, 9] while the electronic conductivity of the catalyst can normally be enhanced via the combination of the catalytic active components with electronic conductive substrates such as carbon nanotubes, graphene and so on.[10, 11] On the other hand, cobalt sulfide is a typical kind of transition metal chalcogenide which is earth abundant and frequently exhibits good OER activities.[12] It is, therefore, anticipated that a composite containing cobalt sulfide and tungsten sulfide as well as conducting carbon substrate

is potential bifunctional electrocatalysts towards both HER and OER. However, such a complex composite is difficult to generate via conventional material process methods, not to mention the desire of homogeneous nanostructures that could expose more catalytic active sites and enable better mass transport for the reactions of interest. Nevertheless, some recent reports have shed some light in this aspect. For instance, Shang et al. synthesized  $\text{Co}_x\text{S}_y$ -incorporated  $\text{WS}_2$  nanosheets supported on a pre-treated hydrophilic carbon cloth via a hydrothermal synthesis route;[13] Similarly, Liu et al. prepared ternary hybrid cobalt disulfide-molybdenum disulfides supported on carbon nanotubes composite via a simple hydrothermal method.[14] Moreover, Zhou et al. also report to produce a composite including  $\text{CoS}_2$  and  $\text{WS}_2$  coated carbon fiber cloth via a three steps synthesis method which involved the use of electrodeposition, drop coating and CVD sulfurization.[15] However, the components in these complicated composites are in general less homogeneous presented in the samples, and only HER performances of these composites were evaluated.[13-15]

In recent decade, Zeolitic imidazolate frameworks (ZIFs) have been ardently investigated as sacrificial templates for various complex composites due to their natural compositions, porous structures and easy tailorability. ZIFs are a special kind of metal organic frameworks (MOFs) with zeolite-like highly porous structures assembled from metal ions and organic ligands. The possibility of metal nodal substitution has make them a versatile precursor to multi-metallic compound-carbon composites;[16, 17] Moreover, the “small mouth, big belly” porous cages of ZIFs or MOFs not only offer an unique opportunity to immobilize metal nanoparticle clusters or catalytic active species with appropriate sizes,[18-20] but also open up an alternative way to introduce metal species that are inherently incompatible with metal nodal substitution method,

leading to complex functional composites which have many advantages when used as catalysts, but difficult to produce via traditional routes.

Given that ZIF-67 possesses a sodalite zeolite-type structure with cavity size of 1.14 nm and aperture size of 0.33 nm,[21] it is potentially an excellent porous host to confine specific molecular structures with sizes larger than its aperture size. This has been actually demonstrated that ZIF-67 can perfectly encapsulate Keggin-type polyoxometalate (POM) clusters, such as phosphotungstic acid (PTA), which can readily hydrolyze into Kegging type  $\alpha$ -PW<sub>12</sub>O<sub>40</sub><sup>3-</sup> with size of 1 nm,[22] and remain stable in the cages of MOFs without leaching during the hydrothermal synthesis of POM@MOF composite. The produced POM@MOF composites, which are characterized with the combination advantages of both MOFs and POMs, together with homogeneous distribution of the POM clusters within the 3D MOF matrix, have attracted increased interest in the past several years,[23, 24] due to their great capability to provide not only the regular arranged organic linkers but also W, Mo, etc. sources that can result in the generation of W or Mo-based electrochemical active catalysts on porous carbons with high specific surface areas via carbonization process.[25, 26] The generated composites are mainly transition metal carbides or oxides particles homogeneously distributed on porous carbon materials and showed much improved electrocatalytic performance in HER,[25-29] due to the fact that the in-situ formed porous carbon substrates can not only remarkably increase the electronic conductivity of the composites, but also efficiently prevent the agglomeration of the electrocatalytic active metal carbide or oxide particles.[28, 29]

In this work, for the first time, we presented a facile one-step sulfurization/ carbonization approach to produce bimetallic tungsten-cobalt sulfide-based on heteroatom doped porous carbon (WS<sub>2</sub>/ Co<sub>1-x</sub>S@N, S co-doped porous carbon) nanocomposites utilizing the in-situ

synthesized PTA@ZIF-67 as precursors, where the PTA can provide abundant tungsten source, metal ion in ZIF-67 acts as cobalt source while the organic linker in ZIF-67 is the source of carbon substrate. The homogeneous confinement of PTA molecular clusters in ZIF-67 can eventually lead to the formation of a homogenous dispersion of tungsten sulfide and cobalt sulfide particles within the ZIF-derived 3D porous carbon matrix after heat treatment in H<sub>2</sub>S atmosphere. The resulting bimetallic Co-W sulfides/porous carbon composites not only exhibit the prominent improvement in electrocatalytic activities towards both HER and OER, but also show increased stability in electrocatalytic performance due to the effective prevention of the agglomeration of metal sulfide particles via the in-situ formed porous carbon matrix.

## **2. Experimental section**

### **2.1 Chemicals**

2-Methylimidazole (99%, abbreviated as MeIM), Cobalt nitrate hexahydrate (Co(NO<sub>3</sub>)<sub>2</sub>·6H<sub>2</sub>O) and Phosphotungstic acid hydrate (H<sub>3</sub>PW<sub>12</sub>O<sub>40</sub>·xH<sub>2</sub>O, abbreviated as PTA) were bought from Sigma-Aldrich and used without further purification.

### **2.2 Materials synthesis**

ZIF-67 was synthesized by hydrothermal method in an aqueous solution. 1.125 g Co(NO<sub>3</sub>)<sub>2</sub>·6H<sub>2</sub>O and 13.75 g MeIM were dissolved separately in distilled water (with total amount of 57.5 ml) before mixing together under magnetic stirring at room temperature for 24 h. The resulting mixture was centrifuged to separate the purple ZIF-67 and the solution. ZIF-67 was then washed with water and methanol each for three times to remove the excess MeIM. Finally,

the purple powder was separate from the solution by centrifuge (7000 rpm, 10 min) and dried in a fuming cupboard for several days before subject to further heat treatment.

The synthesis of PTA@Z67 was similar to the synthesis procedure of ZIF-67, except that PTA was dissolved in water together with  $\text{Co}(\text{NO}_3)_2 \cdot 6\text{H}_2\text{O}$  before mixing with MeIM solution. Three composites with different amount of PTA (1.113 g, 0.557 g and 0.371 g) were synthesized. The resulting samples were denoted as W30@Z67, W20@Z67 and W10@Z67 respectively.

To obtain porous carbon composite, 0.2 g dried sample powder in a ceramic boat was put in a horizontal flow-through quartz tube in a tube furnace. Samples were heated to different temperatures (600, 800 and 1000 °C) at a heating rate of 10 °C min<sup>-1</sup> under Argon atmosphere. After reaching the target temperature, hydrogen sulfide gas at flow rate of 50 mL min<sup>-1</sup> was introduced to sulfurize the sample and this process was maintained for 1 h. After 1 h, H<sub>2</sub>S was switched off and the furnace was allowed to cool down naturally to room temperature under Ar flow. The final product was labelled as xWZ-y, where *x* is the ratio of Cobalt nitrate hexahydrate to PTA and *y* is the heat treatment temperature. For example, 20WZ-800 stands for the sample obtained by heat treatment of the precursor sample W20@Z67 at 800 °C. For comparison, PTA-800 was also produced by heat treatment of net PTA at 800 °C for 1 h in H<sub>2</sub>S atmosphere.

### 2.3 Material characterizations

Fourier-transform infrared (FT-IR) spectra were recorded in the wavelength range of 500-1300 cm<sup>-1</sup> on Shimadzu IRTracer-100 spectrometer, and samples were prepared by KBr pellet method. X-ray diffraction (XRD) patterns were obtained with Bruker D8 advanced X-ray diffractometer with Cu-K $\alpha$  radiation at 40 mA and 40 kV. Scanning electron microscopy (SEM) images were taken with a Helios Nanolab 600i scanning electron microscope/Focused ion beam DualBeam workstation at an acceleration voltage of 10 kV. Samples were coated with 10 nm of

gold to reduce the effects of charging. Transmission electron microscopy (TEM) images were obtained by a JOEL-2100 LaB6 transmission electron microscope. Samples were dispersed by sonication in absolute ethanol for 10 min and were deposited on a holey carbon copper grid and dried overnight before TEM analysis. Some samples were subject to thermogravimetric analysis (TGA) using a TA SDT Q600 instrument with target temperature of 800 °C, heating ramp of 10 °C min<sup>-1</sup> and Air flow rate of 100 mL min<sup>-1</sup>. N<sub>2</sub> gas sorption analysis was carried out for material texture analysis on a Quantachrome Autosorb-iQ gas sorptometer by using conventional volumetric technique. Before the actual gas analysis, samples were outgassed under vacuum at 150 °C for 3 h. Brunauer-Emmett-Teller (BET) method was used to calculate the surface area of the samples. Adsorption data in the partial pressure (P/P<sub>0</sub>) range of 0.05-0.2 was used for the calculation. Total pore volume was determined from the amount of adsorbed N<sub>2</sub> at P/P<sub>0</sub> ca. 0.99. Raman spectra were acquired with Renishaw inVia Raman microscope using a 20X objective lens and an excitation laser beam of 532 nm in wavelength. X-ray photoelectron spectroscopy (XPS) was performed on a Kratos Axis Ultra system with a monochromated Al Kr X-ray source operated at 10 mA emission current and 15 kV anode potential.

## **2.4 Electrocatalytic measurements**

Electrochemistry measurements were carried out on a CHI660E electrochemical workstation at room temperature. The rotating disk electrode (RED) measurements were performed with the help of CHI 760D potentiostat. A classic three electrode electrochemical set up was used. Pt wire and Ag/AgCl electrode were used as the counter and reference electrodes respectively. 1 M KOH solution and 0.5 M H<sub>2</sub>SO<sub>4</sub> solution were used as electrolyte for OER and HER analysis respectively. For the OER test, O<sub>2</sub> was purged into the electrolyte for 20 min in advance and kept purging during the test to form a O<sub>2</sub>-saturated KOH solution. To prepare the working electrode,

a glassy carbon (GC) electrode (3 mm in diameter) was first polished with 0.05  $\mu\text{m}$  alumina slurries on a BAS Diamond polishing pad then on BAS Alumina polishing pad to obtain a mirror-like finish. After polishing, the electrodes were cleaned with distilled water. To prepare the sample ink, 3 mg of catalyst was dispersed in 1 mL of water-ethanol (4:1 v/v) solution with additional 5  $\mu\text{L}$  of 5wt% Nafion solution by ultrasonic bath for 30 min. Afterwards 5  $\mu\text{L}$  of the resulting suspension was deposited onto the polished glassy carbon (GC) electrode with the aid of Eppendorf micropipette. The ink on the electrode was then let dry naturally and overnight. The loading of each catalyst is calculated to be approximately 21 mg /cm<sup>2</sup> based on above ink preparation.

To prevent bubbles on the electrode-electrolyte interface, a drop of distilled water was added onto the electrode before immersed into the electrolyte. All potentials were measured vs. the Ag/AgCl reference electrode and reported vs. the reversible hydrogen electrode (RHE). The conversion of  $E_{(\text{Ag}/\text{AgCl})}$  to  $E_{(\text{RHE})}$  was calculated with Nernst equation:

$$E_{(\text{RHE})} = E_{(\text{Ag}/\text{AgCl})} + 0.059 \times (\text{pH}) + 0.197$$

where pH is the pH value of the electrolyte solution. For 0.5 M H<sub>2</sub>SO<sub>4</sub> and 1 M KOH solution, the pH value is 0 and 14 respectively.

Due to the effect of ohmic resistance on intrinsic catalytic activity, all the polarization curves are presented with iR compensation for further analysis. The compensation was automatically applied by the software with a compensation level of 95%.

### **3. Results and discussion**

#### **3.1 Characterization of as-made PTA@Z67**

PTA@Z67 hybrids were first synthesized through an in-situ self-assembly of 2-methylimidazole (MeIM), cobalt nitrate hexahydrate and phosphotungstic acid hydrate (PTA) in

one pot, followed by heat treatment of the in-situ formed PTA@ZIF-67 in H<sub>2</sub>S atmosphere at higher temperature to generate the bimetallic tungsten-cobalt sulfide on heteroatom doped porous carbon nanocomposite, as schematic demonstrated in Fig. 1. Due to the acidic sensitivity of ZIF-67, excess amount of MeIM was necessary to buffer the acidity of PTA.[30] Therefore, a green aqueous synthesis method which required large amount of MeIM[31] to in-situ synthesize PTA@ZIF-67 was adopted in this study. This simple, facile and environmentally friendly synthesis method enables to prepare gram-scale precursor products efficiently.

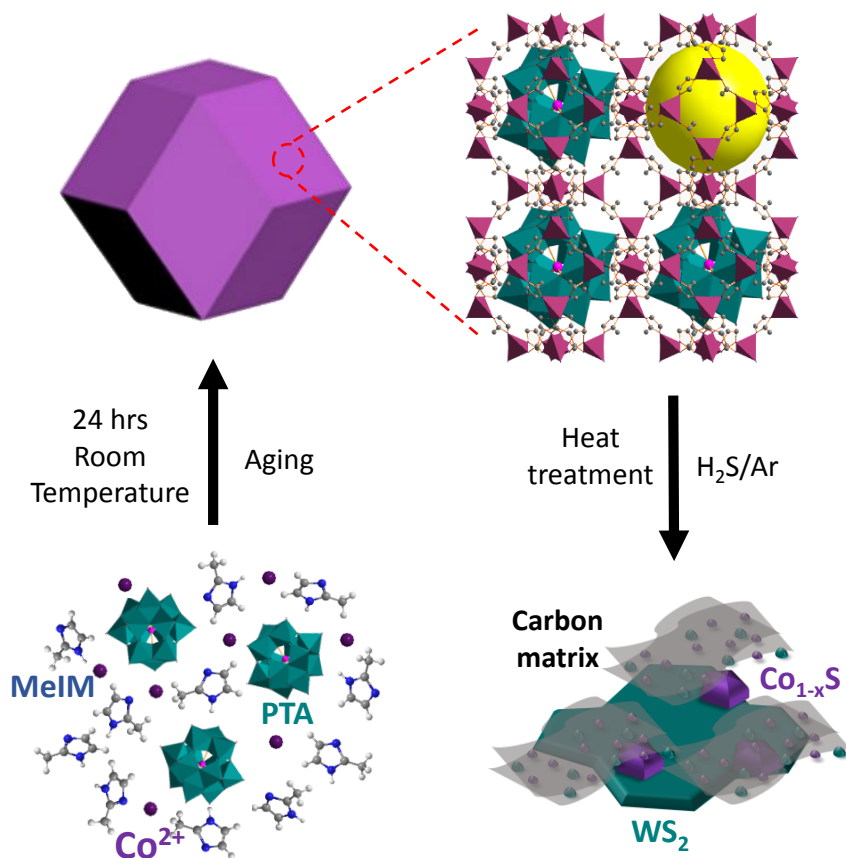


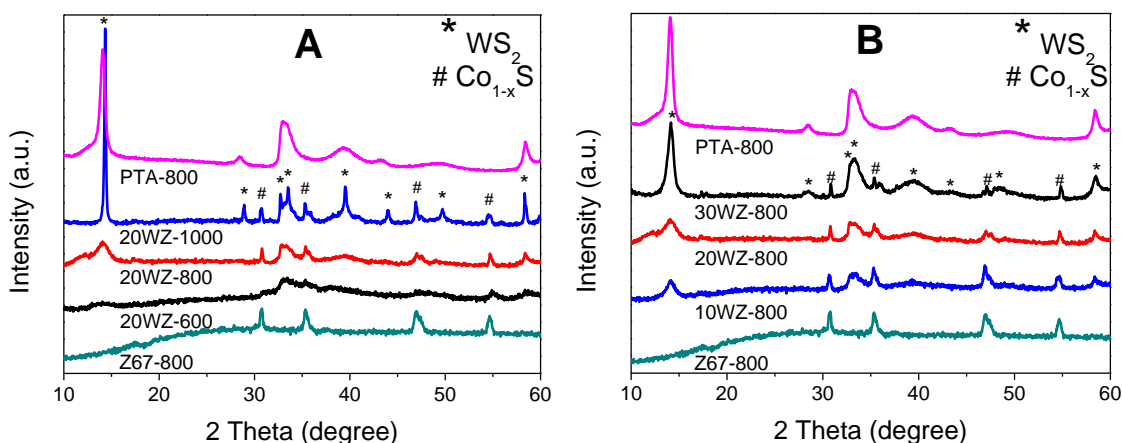
**Fig. 1** Schematic diagram of the preparation of WS<sub>2</sub>/ Co<sub>1-x</sub>S@N, S co-doped carbon nanocomposite.

The structures of the as-made PTA@Z67 were characterized and presented in the Supporting Information (SI). FT-IR spectra (SI Fig. S1) confirms the existence of PTA in the synthesized PTA@Z67 samples while powder XRD (SI Fig. S2) demonstrates that the introduction of PTA can affect the formation of ZIF structures, but the incorporation of controlled amount of PTA into the products can maintain the well-defined ZIF-67 structures and the PTA may be well confined in the cages of ZIF-67 as no characteristic diffraction peaks of PTA can be identified in the XRD measurement results. TGA curves (SI Fig. S3) clearly show that PTA has been successfully introduced in the resulting as-synthesized precursors, evidenced by the elevated remaining weight for the increased PTA amount used during the synthesis. In addition, N<sub>2</sub> gas sorption analysis results (SI Table. S1) further confirm that the PTA molecules are encapsulated in the pore channels and/or some cages of ZIF-67 which results in the decrease in surface area and pore volume of the precursors. Therefore, all the analysis results suggested that PTA molecules have been successfully encapsulated within the sodalite (SOD) cages of ZIF-67 without dramatically altering its 3D structures. The obtained PTA@ZIF-67 were then subject to heat treatment in Ar/H<sub>2</sub>S mixed gas atmosphere at 600, 800 and 1000 °C respectively for 1 h to generate W,Co sulfide/N,S co-doped carbon nanocomposites.

### **3.2 Characterization of PTA@Z67 derived nanocomposites**

The XRD patterns of the composites obtained by heat treatment of W20@Z67 under different heat process temperature of 600, 800 and 1000 °C respectively are shown in Fig. 2A. For comparison, the XRD patterns of samples Z67-800 and PTA-800 prepared by heat treatment of pristine ZIF-67 and pure PTA under the same atmosphere at 800 °C are also included. While sample PTA-800 exhibited diffraction peaks similar to the patterns of IF-WS<sub>2</sub> (JCPDS No. 08-

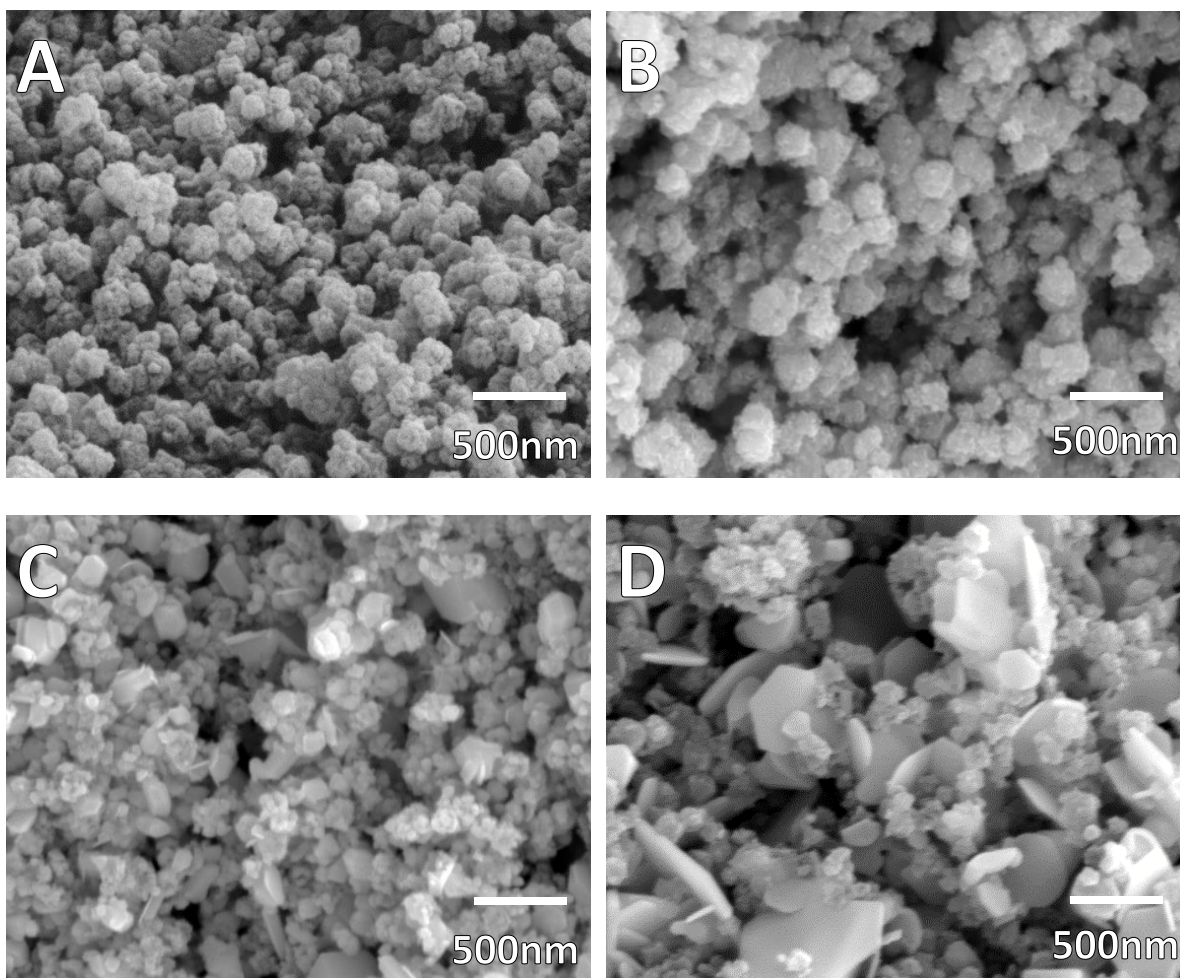
0237),[32] the XRD patterns of the PTA modified composites mainly show diffraction peaks indexed to  $\text{Co}_{1-x}\text{S}$  (JCPDS No. 42-0826)[33] and  $\text{WS}_2$ . Moreover, the sharpness and the intensity of the cobalt sulfide and tungsten sulfide peaks increase with the increase of heat process temperature, suggesting that higher heat process temperature results in higher crystallinity of metal sulfides. There is no observable diffraction peak at  $2\theta$  of  $26^\circ$ , maybe due to the amorphous nature of the carbon with lower diffraction intensity compared with crystalline sulfides.



**Fig. 2** XRD patterns of different nanocomposites. A). PTA-800, 20WZ-1000, 20WZ-800, 20WZ-600 and Z67-800. B). PTA-800, 10WZ-800, 20WZ-800, 30WZ-800 and Z67-800.

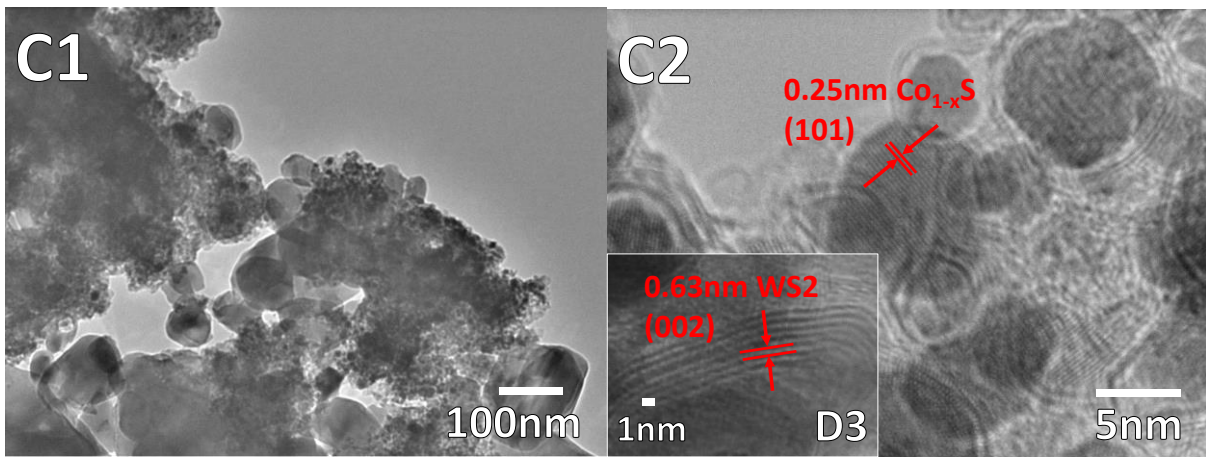
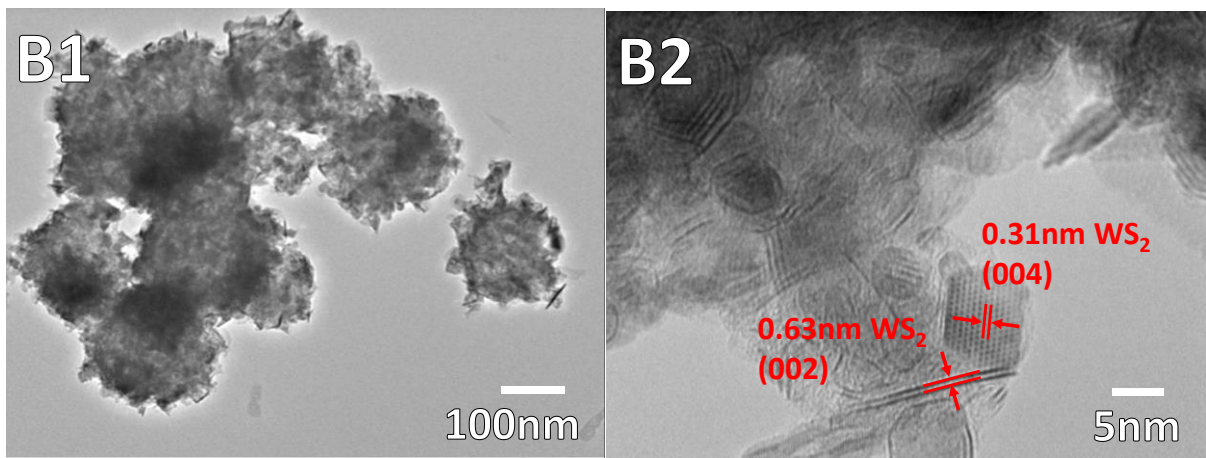
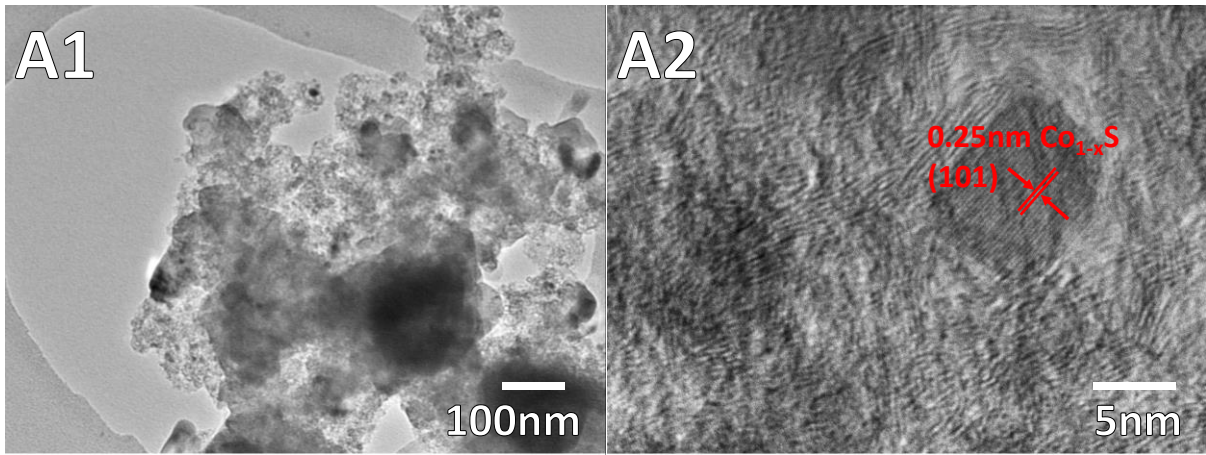
The representative SEM images of Z67-800 and the heat treated W20@Z67 in  $\text{H}_2\text{S}$  atmosphere at various temperatures are shown in Fig. 3. Comparing with the pristine ZIF-67 (see SI Fig. S4A), the composite derived from ZIF-67 (sample Z67-800 in Fig. 3A) largely retains the shape and size of its precursor, but shows a lumpy surface. As heat treatment temperature increased,

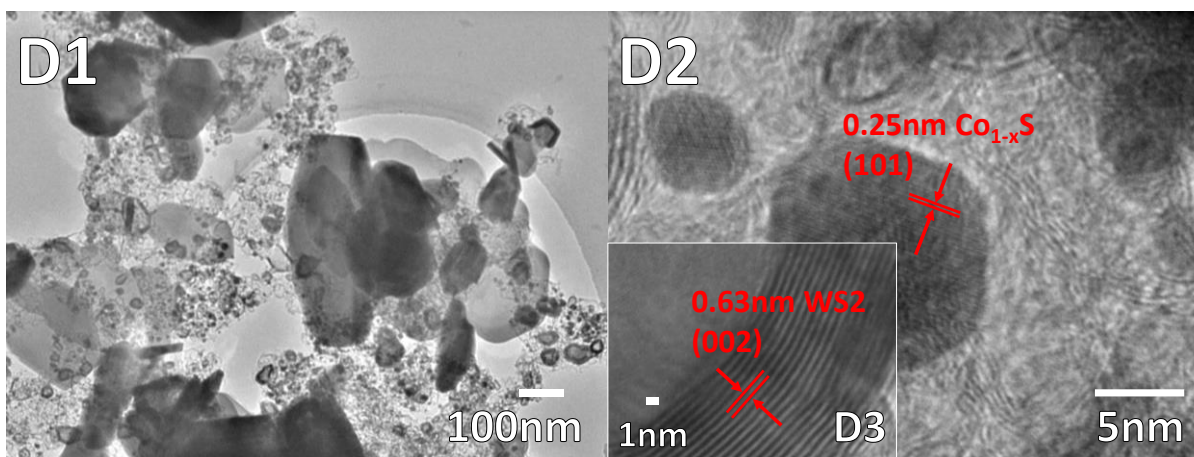
the particles have gradually shrink and collapsed to smaller particles with rough surfaces (Fig. S4B and C). In contrast, PTA modified composite obtained at 600 °C (sample 20WZ-600) displays a larger particle shape and size but a downy surface (Fig. 3B). At 800 °C the particles in sample 20WZ-800 were collapsed and large amount of small flakes with size of around 100 nm has appeared between smaller downy particles (Fig. 3C). As temperature increased to 1000 °C, the size of thin flakes in 20WZ-1000 grows up to 1  $\mu\text{m}$  (Fig. 3D). These observations clearly imply that the morphologies of the W20@Z67 derived composites can be remarkably affected the heat process temperature of the samples.



**Fig. 3** Representative SEM images of different nanocomposites. (A) Z67-800, (B) 20WZ-600, (C) 20WZ-800 and (D) 20WZ-1000.

Fig. 4 presents the typical TEM images of Z67-800, 20WZ-600, 20WZ-800 and 20WZ-1000. As shown in Fig. 4A1, only a small amount of black cobalt sulfide particles are clearly observed in Z67-800. The d-spacing between the lattice fringes of (101) for cobalt sulfide in the composite Z67-800 is calculated to be 0.25 nm (Fig. 4A2), which interactively agreed with the value obtained from the XRD results in Fig. 2A. However, in the 20WZ series composites derived from heat process of 20W@Z67 in H<sub>2</sub>S atmosphere at high temperatures (Fig. 4 B1-D1), there are obviously more metal sulfide black particles. In addition, both the amount and the size of the black particles increase with the heat process temperature. High magnification TEM images (Fig. 4B2-D2) clearly exhibit the lattice fringes of 6.3 Å and 3.1 Å which corresponds to the (002) and (00) planes of 2H-WS<sub>2</sub> respectively for all three 20WZ samples obtained under different heat treatment temperatures, confirming the existence of WS<sub>2</sub> flakes. Moreover, apart from the WS<sub>2</sub> particles, composites 20WZ-800 and 20WZ-1000 obtained by heat treatment of 20W@Z67 at 800 and 1000 °C (Fig. 4C2 and D2) also confirm the presence of Co<sub>1-x</sub>S particles with d-spacing of 0.25 nm for the (101) crystalline planes. These TEM images are in very good agreement with the aforementioned XRD and SEM results. In particular, the general shape of ZIF-67 crystal is more or less still observable in the 600 °C heat processed sample (Fig. 4B1) as the formation of tiny flaky WS<sub>2</sub> brings a downy effect to the surface of the particles. With increase of the pyrolysis temperature, both Co and W bimetallic sulfides with improved crystallinity are formed evidenced by both the increased XRD peak intensities in Fig. 2 and the observed fringes for both cobalt sulfide and tungsten sulfide in Fig. 4C2 and D2, leading to significant changes in morphologies of these samples.

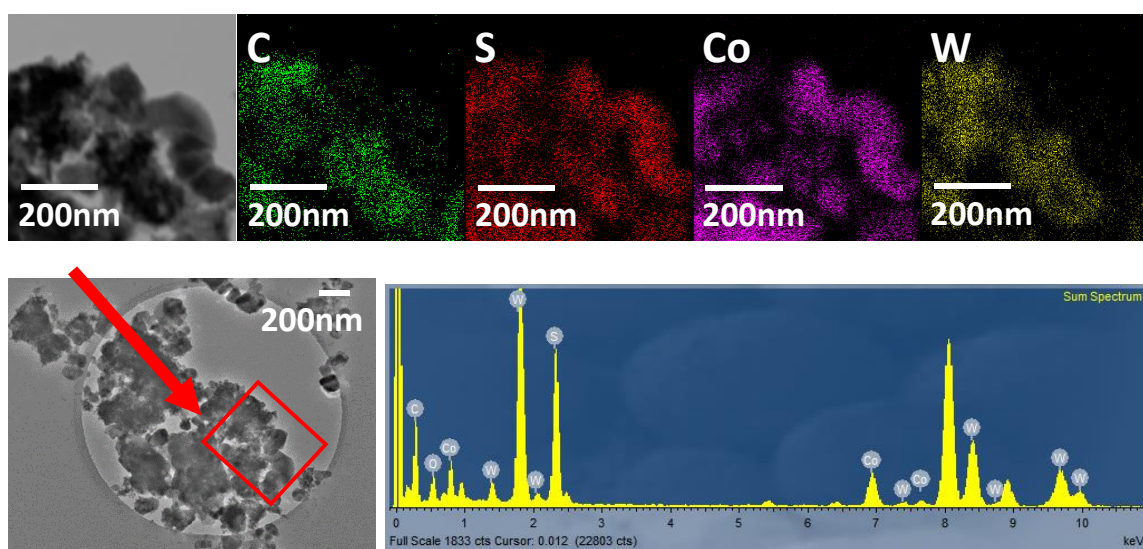




**Fig. 4** Representative TEM images of different nanocomposites. A) Z67-800, B) 20WZ-600, C) 20WZ-800 and D) 20WZ-1000.

Moreover, sample 20WZ-800 (Fig. 4C1), shows large particles outside the carbon matrix with sizes approximately in the range of 50-100 nm, which possibly originates from the migration and agglomeration of small metal sulfide particles within carbon matrix driven by thermal gradient during the heat process. HRTEM image of this sample in Fig. 4C2 and SI Fig. S5B indicates that there are small  $\text{Co}_{1-x}\text{S}$  spheres and onion-like inorganic fullerene (IF- $\text{WS}_2$ ) particles with size of around 5-10 nm embedded in an in-situ formed carbon matrix derived from the carbonization of the organic linkers in  $\text{W20@Z67}$ . As the heat treatment temperature increases to 1000 °C, the resulting sample 20WZ-1000 (as shown in Fig. 4D2 and SI Fig. S5C) displays larger  $\text{Co}_{1-x}\text{S}$  particles in the carbon matrix with size up to 15 nm in diameter, meanwhile the number of onion layers of the carbon wrapped IF- $\text{WS}_2$  particles have increased as well. It is believed that the confined molecular PTA clusters within the ZIF-67 cages could first decompose to tungsten oxide species at high heat process temperatures, the formed tungsten species then react with  $\text{H}_2\text{S}$  gas to form layer  $\text{WS}_2$  particles. The formation of this layer  $\text{WS}_2$  structure may be based on the outside-in growth mechanism proposed by Feldman et al. that the S atom and H atom

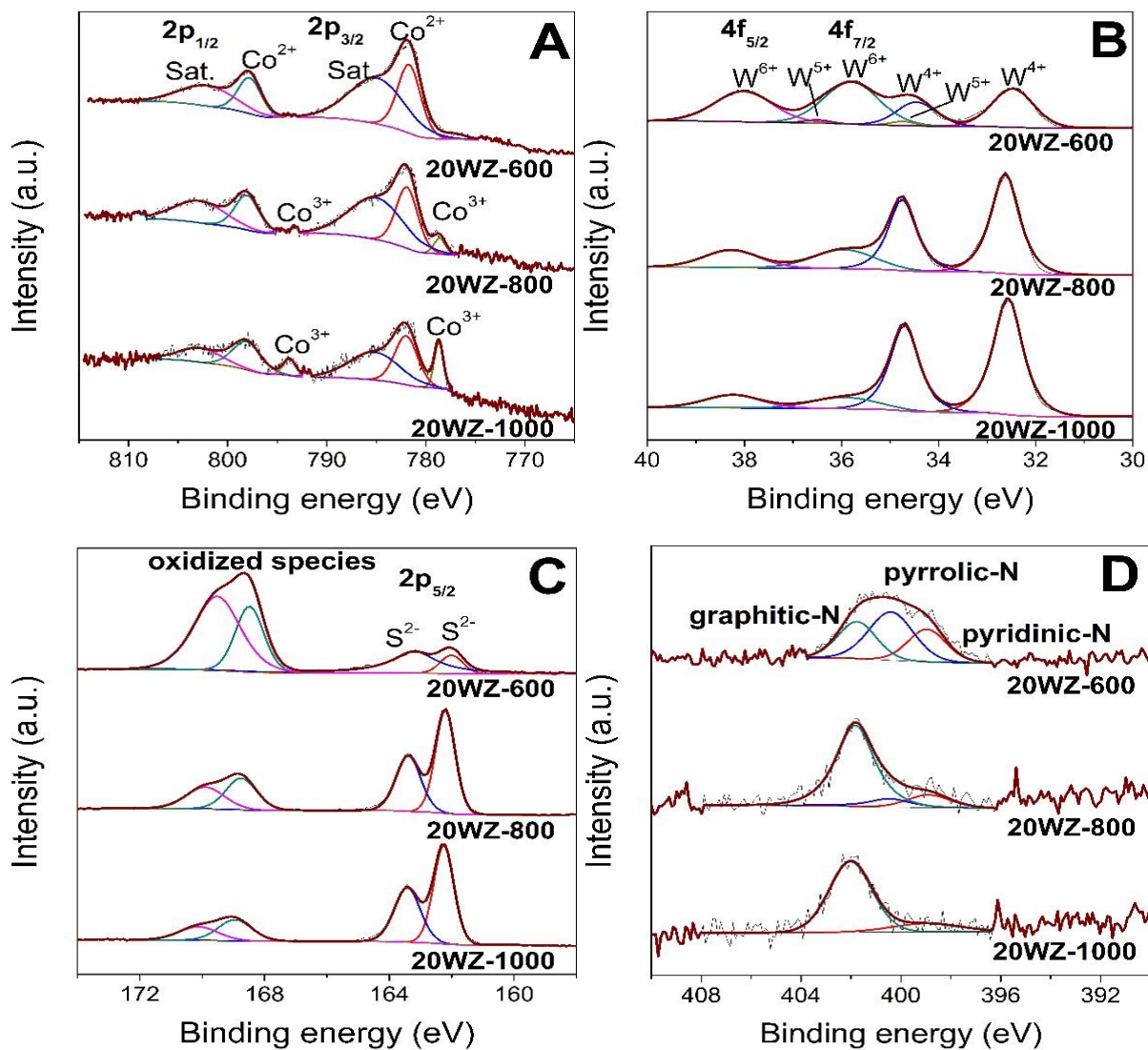
decomposed from  $H_2S$  will diffuse into and react with the as-formed nanoparticle of  $WO_x$  to further produce layers of  $WS_2$ . [34, 35] The O atoms in the tungsten oxide nanoparticles will be gradually replaced by S atoms and eventually a  $WS_2$  onion ball (IF- $WS_2$ ) is formed. At higher heat process temperatures, large  $WS_2$  flakes with size up to  $1\ \mu m$  is formed (see both Fig. 3C, D and SI Fig. S5C). In addition, large  $Co_{1-x}S$  crystals with a size up to 200 nm also grow along outside the carbon matrix, which result from the migration and agglomeration of  $Co_{1-x}S$  nanocrystals under heat treatment process (as shown in both Fig. 4 and SI Fig. S5B and C).



**Fig. 5** TEM images, elemental mappings and element spectrum of 20WZ-800.

To gain more information on the surface composition and chemical state of the as-synthesized nanocomposites, TEM-EDX and XPS analysis were performed and the results are shown in Fig. 5 and 6, respectively. The elemental mappings and EDX spectrum in Fig. 5 and SI Fig. S6 clearly confirm the presence of C, S, Co and W in the composite, which is consistent with the XRD. In addition, the elements distribution mappings together with the corresponding TEM image have suggest the homogeneous distribution of all the elements in the samples. Element

survey carried out on XPS and presented in SI Fig. S7 further confirms the presence of W, Co, S, C, N and O in all the PTA@ZIF-67 derived composites. High resolution XPS spectra of N 1s and C 1s (Fig. 6D and E) have suggested that the carbon matrix was co-doped with N and S.



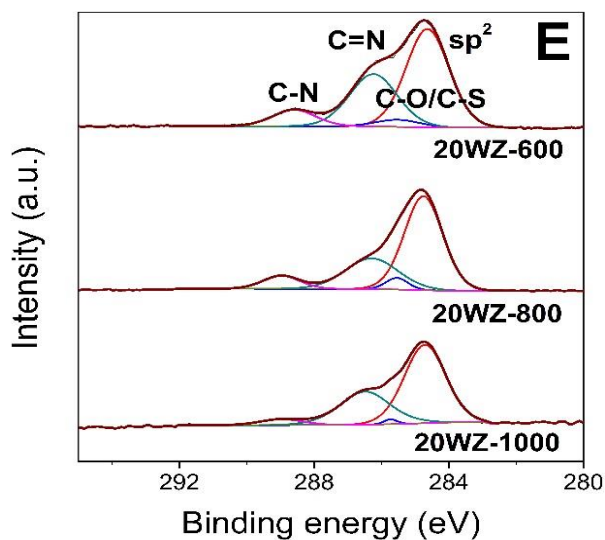


**Fig. 6** High-resolution XPS spectra of A) Co 2p, B) W 4f, C) S 2p, D) N 1s and E) C 1s for 20WZ-600, 20WZ-800 and 20WZ-1000.

Fig. 6A presents the high-resolution XPS spectra of Co 2p for 20WZ obtained at 600, 800 and 1000 °C respectively. The two spin-orbit doublets peaks at approximately 781.8 (2p 1/2) and 798.1 eV (2p 3/2) are the characteristics of  $\text{Co}^{2+}$  oxidation state in the surface species, belonging to the Co-S bond due to the formation of  $\text{Co}_{1-x}\text{S}$ . [36] While the peaks at around 785 and 802 eV are the corresponding shake-up satellite peaks, [37] the two spin-orbit doublet peaks at around 793.7 (2p 1/2) and 778.7 eV (2p 3/2) only observable for sample 20WZ-800 and 20WZ-1000 can be ascribed to  $\text{Co}^{3+}$  oxidation state. It is therefore suggested that mixed oxidation states (both  $\text{Co}^{2+}$  and  $\text{Co}^{3+}$ ) existed in high temperature derived samples, which is consistent with previous report. [33] Moreover, comparing the XPS spectra of Z67-800 with that of 20WZ samples, the 2p 3/2 peak for  $\text{Co}^{3+}$  and  $\text{Co}^{2+}$  has shifted from 778.4 and 781.9 eV (Z67-800) through 778.5 and 781.7 eV (20WZ-800) to 778.7 and 781.8 eV (20WZ-1000) respectively (SI Fig. S8), which is very close to the Co 2p spectra of Co-W-S phases at 778.6~778.8 eV, [38, 39] indicating an increasing strong interaction between  $\text{Co}_{1-x}\text{S}$  and  $\text{WS}_2$  as temperature increases.

Moreover, in the W 4f spectrum shown in Fig. 6B, all the 20WZ samples can be deconvoluted into four peaks. Peaks at around 38.0 (4f 5/2) and 35.8 eV (4f 7/2) indicate the presence of W<sup>6+</sup> species,[40] which could be due to the thermal decomposition intermediates of PTA. At high temperature in H<sub>2</sub>S atmosphere, the W<sup>6+</sup> species will gradually react with H<sub>2</sub>S gas to form WS<sub>2</sub>, hence the relative intensity of W<sup>6+</sup> peaks decreases with increasing temperature. The other two peaks at around 34.7 (4f 5/2) and 32.6 eV (4f 7/2) indicate the presence of W<sup>4+</sup> species which could be assigned to the formed WS<sub>2</sub>. [39] This result is also in line with above XRD results. The relative area of the W<sup>4+</sup> species are much bigger for the 800 and 1000 °C samples compared with the 600 °C one, which clearly suggests that under relatively high pyrolysis temperature in H<sub>2</sub>S atmosphere, more WS<sub>2</sub> formed from W<sup>6+</sup> species. It is worth to mention that 20WZ-600 exhibits an extra pair of weak peaks at 36.50 and 34.73 eV, which can be assigned to W<sup>5+</sup>, indicating the presence of oxygen vacancies in the WO<sub>x</sub> precursor,[41] possibly from the decomposition intermediate of PTA.

In addition, high resolution XPS spectra for S 2p are shown in Fig. 6C. The peaks observed at around 162.2 and 163.39 eV are corresponding to the S 2p<sub>5/2</sub> and S 2p<sub>3/2</sub> doublets with a binding energy separation of 1.19 eV, corresponding to the S<sup>2-</sup> species of WS<sub>2</sub>. [42, 43] The second pair peaks located at around 168.8 and 169.9 eV are assigned to the S 2p<sub>3/2</sub> and S 2p<sub>1/2</sub> peaks of oxidized S species, such as sulfate groups,[44] which could be due to the oxidation of sulfur in air,[45] or intermediate products formed during the transformation of WS<sub>2</sub> from PTA and H<sub>2</sub>S. At lower pyrolysis temperature in H<sub>2</sub>S, the oxidized S species are dominant in sample 20WZ-600. However, with increase of the pyrolysis temperature, WS<sub>2</sub> gradually turn to be dominant component in the sample 20WZ-800 and 20WZ-1000, consequently the peak areas for S<sup>2-</sup> species are much larger in the 800 and 1000 °C samples than that in the 600 °C sample.

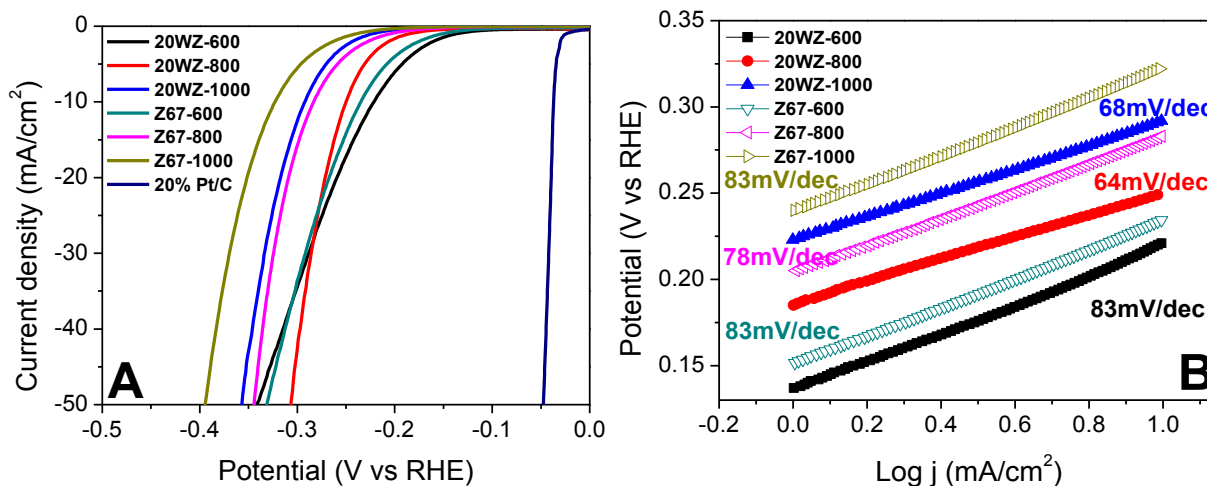
The Raman spectra in SI Fig. S9 shown that all three bi-metallic composites clearly present G band and D band at 1590 and 1340  $\text{cm}^{-1}$  respectively. The G band suggested the existence of non-crystalline carbons and  $\text{sp}^2$ -hybridized carbon atoms resulted from the carbonization of the samples, while D band indicated the presence of a more ordered carbon.[46] The relative intensity of two peaks, i.e.  $I_D/I_G$ , has increased with increased temperature, indicating the increased amount of edge and topological defects with higher carbonization/sulfurization temperatures.[47]

Moreover, gas sorption analysis of the sulfurized tungsten modified samples shows that an increasing in specific surface area and total pore volume (as shown in SI Table S2), which may be due to the migration and agglutination of nano size metal sulfide from the carbon matrix to the surrounding leaving pores behind in the carbon matrix.

### **3.3 Electrocatalytic performance of generated materials**

The electrochemical performance of the produced  $\text{WS}_2/\text{Co}_x\text{S}_y@\text{N,S}$ -codoped carbon nanocomposites are evaluated as electrocatalysts at room temperature in a three-electrode setup. 0.5 M  $\text{H}_2\text{SO}_4$  electrolyte was used for HER test. To be more prudent, in this study the commonly reported potential at current density of 10  $\text{mA cm}^{-2}$  is adopted for comparison[48] and the relevant HER measurement results are presented in Fig. 7 and SI Table S3. It is clear that sample 20WZ-600 shows the lowest potential of 0.221 V (vs. RHE) to achieve current density of -10  $\text{mA cm}^{-2}$  amongst all the W-modified samples (as shown in Fig. 7A and SI Table S3); however it does not show higher current density as voltage increases. The early start of the HER may be ascribed to the oxygen vacancies existed in the intermediate non-stoichiometric tungsten oxide,[49, 50] which was proofed by the XPS result earlier. As the reaction continues, the non-stoichiometric compound is gradually oxidized to form stoichiometric tungsten oxide,  $\text{WO}_3$ . The

increased  $\Delta G_H$  and inferior electrical conductivity of  $WO_3$  results in degrading electrocatalytic activities as evidenced by the gradual gradient of the polarization curve.[50] The HER activities at higher voltage could be due to the activate site provided by the  $WS_2$  particles imbedded in the carbon matrix as shown in the previous TEM results. The poor crystallinity of carbon could also be one of the reasons for the inferior HER performance. In contrast, 20WZ-800 shows the best overall HER performance with the highest current density at higher potential and it only requires a relatively low potential of 0.250 V (vs. RHE) to reach current density of  $-10 \text{ mA cm}^{-2}$ . By comparing the LSV curves of the modified ZIF-67 derived catalysts and the pristine ZIF-67 derived ones, it is clear that the bimetallic sulfide carbon composite exhibits an overall better HER catalytic activities than the pristine cobalt sulfide carbon composite. In addition, the HER performances of these composites are in general still inferior to the benchmark 20% Pt/C sample.



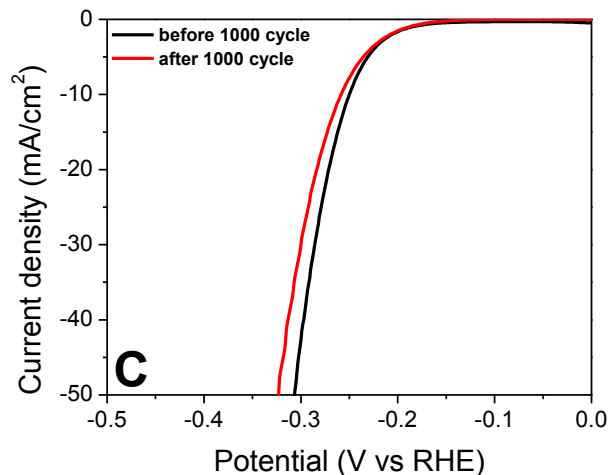


**Fig. 7** A) HER polarization curves of benchmark catalyst 20% Pt/C, carbonized/sulfurised W20@Z67 and ZIF-67 at 600, 800 and 1000 °C; B) The corresponding Tafel plots and C) HER polarization curves of 20WZ-800 recorded before and after 1000 CV cycles. All the polarization curves were iR corrected at a scan rate of 5 mV s<sup>-1</sup> in 0.5 M H<sub>2</sub>SO<sub>4</sub> electrolyte solution.

To better interpret the polarization curve, the reaction mechanism indicator, Tafel slope, was calculated from Tafel equation to evaluate the electrocatalytic activity:

$$\eta = a + b \log(j)$$

Where  $\eta$  is the overpotential,  $j$  is the exchange current density,  $a$  is the interception (i.e.  $\log(j_0)$ ) and  $b$  is the Tafel slope. By plotting the potential versus the current density in logarithm (the so called Tafel plot), and fitting the linear portion of the plot,  $b$  can be easily obtained.[51] The Tafel plots for HER of different samples are constructed based on the corresponding LSV curves in Fig. 7A and are presented in Fig. 7B.

In 0.5M H<sub>2</sub>SO<sub>4</sub> electrolyte, samples Z67-600, Z67-1000 and 20WZ-600 all exhibit a relative high Tafel slope of 83 mV dec<sup>-1</sup>, while Z67-800 shows Tafel slope of 78 mV dec<sup>-1</sup>. However, the corresponding WS<sub>2</sub>/Co<sub>1-x</sub>S@N, S-codoped carbon nanocomposites including both 20WZ-1000

and 20WZ-800 present much lower Tafel slopes. In particular, sample 20WZ-800 exhibits the lowest Tafel slope of  $64 \text{ mV dec}^{-1}$  among all the studied composites and the lowest potential required to achieve current density of  $10 \text{ mA cm}^{-2}$  (see SI Table S3), implying a good HER reaction kinetics of the sample. Actually, the Tafel slope for sample 20WZ-800 surpasses most of reported Co-W-S/C series electrocatalysts in HER (SI Table S4).

The good HER activity is attributed to the novel structure of the composites. The pristine metal sulfides have low conductivity that largely limited their electrochemical performances in HER. However, in the case of 20WZ-800, both  $\text{Co}_{1-x}\text{S}$  and  $\text{WS}_2$  nanoparticles are uniformly dispersed in the heteroatom-doped carbon matrix with  $\text{WS}_2$  being typical HER electrocatalytic component, leading to more active sites in the composites. Moreover, the carbon matrix allows better charge and mass transport between the adsorbed  $\text{H}^+$  and the electrode. In addition, the existence of N species that can result in change in electronic structure of neighbouring carbon atoms, together with the asymmetrical spin and change in charge density originated from the co-doping of N and S, can lead to the increase in the number of active sites[52] and hence enhancement in the HER activity.

Besides the improved HER performance, W20@Z67 derived composites also show promising OER activities. The test was carried out in an oxygen-saturated 1 M KOH aqueous solution at room temperature with electrode spinning rate at 1600 rpm. Fig. 8A presents the linear sweep voltammograms (LSVs) polarization curves of the OER benchmark catalyst  $\text{IrO}_2$ , W20@Z67 and ZIF-67 derived catalysts at different calcination temperatures. To achieve a current density of  $10 \text{ mA cm}^{-2}$ , W20@Z67 derived sample at 600, 800 and 1000 °C requires an overpotential of 0.410, 0.398 and 0.365 V (vs. RHE) respectively, while ZIF-67 derived sample at 600, 800 and 1000 °C needs a higher overpotential of 0.505, 0.440 and 0.396 V (vs. RHE) respectively to

achieve the same current density. Obviously, the incorporation of WS<sub>2</sub> species in the 20WZ series samples dramatically improves the OER performance of the composites. Particularly, the OER activities of all the 20WZ series samples over-perform that of the benchmark IrO<sub>2</sub> catalyst, and 20WZ-1000 exhibits the highest OER performance among all the studied samples and this sample only need the lowest overpotential of 0.365 V (vs. RHE) to achieve the current density of 10 mA cm<sup>-2</sup>.(as shown in SI Table S3)

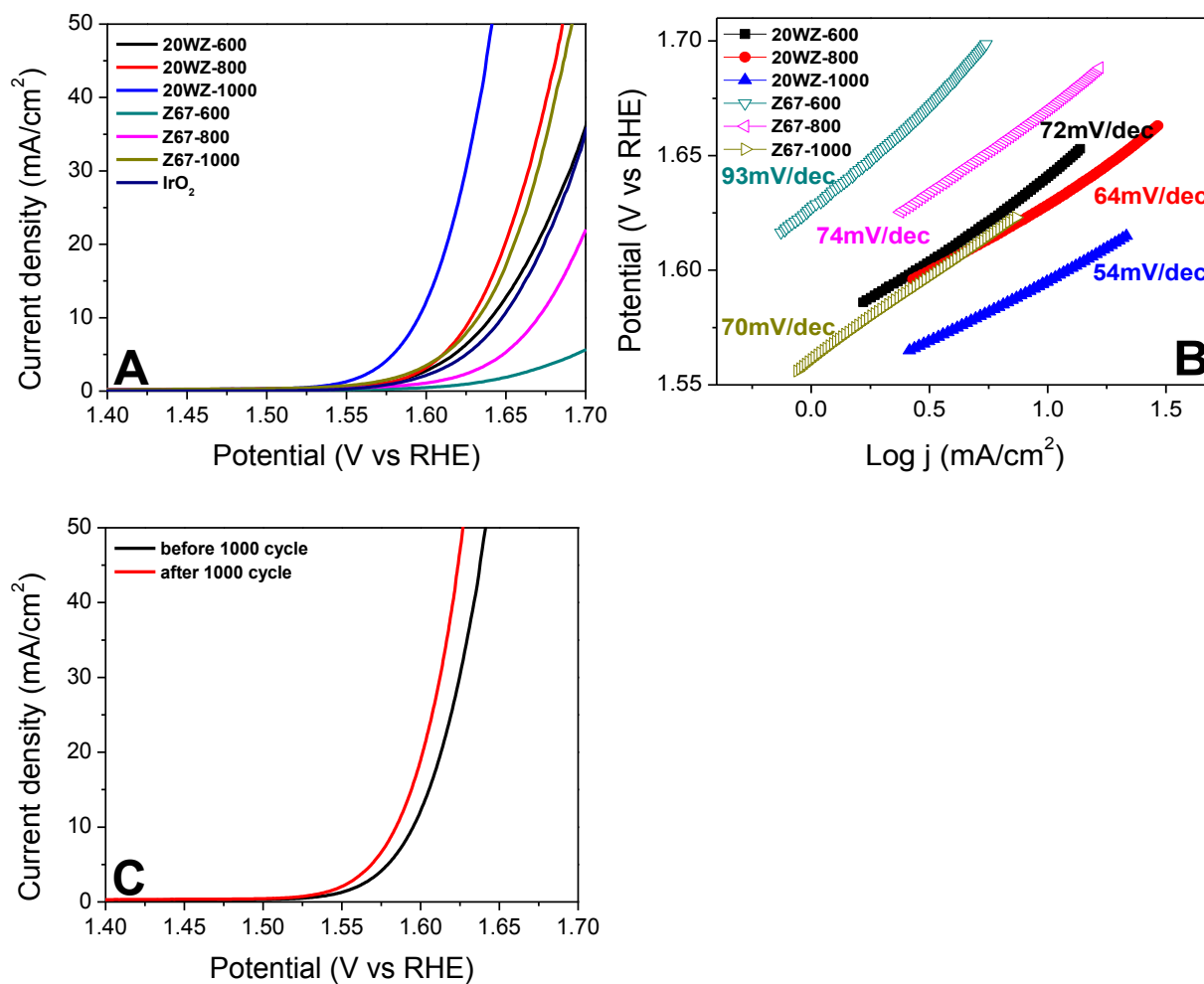


**Fig. 8** A) The LSV polarization curves of benchmark catalysts IrO<sub>2</sub>, carbonized/sulfurised W20@Z67 and ZIF-67 under 600°C, 800°C and 1000°C, B) Tafel plots and C) OER Polarization curves of 20WZ-1000 recorded before and after 1000 CV cycles. All the

polarization curves were iR corrected with a scan rate of  $5 \text{ mV s}^{-1}$  in  $\text{O}_2$ -saturated 1 M KOH electrolyte solution.

The high OER activities of 20WZ-1000 could be due to a number of reasons. Firstly, the presence of defect-rich carbon sites (see Raman spectra in SI Fig. S9) can modulate the electronic and surface properties of the composites, thus change the adsorption energies of electrochemical reaction steps.[53] This is supported by a recent report that suggested defect-rich carbon shows a better electrocatalytic activities than the N doped carbon,[52] which could result in the 1000 °C composite with less N species in the carbon matrix still shows better catalytic activities than the 800 °C sample. Secondly, the generated strong electron transfer between Co and W via the intermediate sulfur atoms, i.e. the formation of Co-W-S phases between the  $\text{Co}_{1-x}\text{S}-\text{WS}_2$  interface, as suggested by Zhang's work.[15] Similar result has been demonstrated by Du et al. in the  $\text{Co}_9\text{S}_8@\text{MoS}_2$  system.[54] Finally, the relative high BET surface area of the 1000 °C sample (see SI Table S2) could also contribute to the high activity by providing loose textures and open space for the easy transportation of evolved gas bubbles and the instant diffusion of the electrolytes, which can help to take the full advantage of active sites in metal sulfides. As the catalyst is a multiphase complicated system, it is however difficult to evaluate the individual composition contribution to the synergistic effect of the catalyst system without disturbing the overall structures.

The corresponding OER Tafel slopes in  $\text{O}_2$ -saturated 1M KOH electrolyte (Fig. 8B) show similar trend to that for HER where the W, Co sulfide-based carbon nanocomposites in general exhibit lower Tafel slopes than their counterparts of ZIF-67 derived samples under the same sulfurization temperatures, clearly indicating that the introduction of  $\text{WS}_2$  into the composite

system results in the remarkable enhancement of the reaction kinetics over their pristine counterparts. Among the W, Co sulfide-based carbon nanocomposites, 20WZ-600 shows the highest Tafel slope of 72 mV dec<sup>-1</sup> and 20WZ-1000 gives the lowest Tafel slope of 53 mV dec<sup>-1</sup>, which even lower than the value for benchmark IrO<sub>2</sub> catalyst (54 mV dec<sup>-1</sup>, see Table S3 in SI), indicating that 20WZ-1000 is the best OER electrocatalyst among all the studied samples, outperforming the benchmark IrO<sub>2</sub> catalyst. The overpotential at 10 mA cm<sup>-2</sup> and Tafel slope data for both HER and OER were summarized and presented in SI Table S3. As a matter of fact, the Tafel slope for sample 20WZ-1000 surpasses many of the reported CoS/C based electrocatalysts in OER (Table S5 in SI).

To examine the HER/OER bifunctional behaviour of the composites, the combined HER and OER LSV curves were presented in SI Fig. S10, where both HER and OER of the representative samples were evaluated in 1 M KOH media. The W-modified sample 20WZ-800 again shows remarkable improved electrochemistry performances both in HER and OER compared with the W-free sample Z67-800. Moreover, sample 20WZ-800 requires a potential of 0.337 V (vs. RHE) to realise a current density of 10 mA cm<sup>-2</sup> in 1 M KOH media for HER, which is merely around 0.087 V reduction for the same composite to achieve the same current density of 10 mA cm<sup>-2</sup> in 0.5 M H<sub>2</sub>SO<sub>4</sub> solution, much smaller than the reduction of potential for benchmark Pt/C catalyst to realise 10 mA cm<sup>-2</sup> in 1 M KOH solution. Obviously, the representative 20WZ-800 sample exhibits good bifunctional electrocatalytic performance towards both OER and HER in alkaline environment.

The kinetics performance of the representative electrode materials was also evaluated by electrochemical impedance spectroscopy (EIS), as presented in SI Fig. S11. The charge transfer resistance ( $R_{ct}$ ) of material can be derived from the diameter of the semi-circle. It is worth noting

that the fast interfacial kinetic is indicated by the small value of the obtained charge transfer resistance. Obviously, 20WZ-800 shows a much smaller  $R_{ct}$  than the Z67-800 sample, which indicated that the introduction of  $WS_2$  into the sample Z67-800 plays a significant role in altering the electronic properties of the composite 20WZ-800. Moreover, benchmark  $IrO_2$  catalyst shows a larger  $R_{ct}$  than 20WZ-800, which is in agreement with the results in LSV curves and Tafel plots.

The stability of the best performed samples, i.e. 20WZ-800 for HER and 20WZ-1000 for OER were evaluated by the LSV curves and the results were presented in Fig. 7C and Fig. 8C. The polarization curve after 1000 cycles is similar to the initial cycle. In particular, the overpotential of 20WZ-800 has dropped only 0.008 V at 10 mA cm<sup>-2</sup> while the overpotential of 20WZ-1000 has slightly increased 0.011 V at 10 mA cm<sup>-2</sup>. The stabilities of both samples were further confirmed by the chronoamperometric curves which were tested at -0.3 V in 0.5 M  $H_2SO_4$  and 0.57 V in 1 M KOH respectively over 8000 s. As shown in SI Fig. S12A and B, sample 20WZ-800 retains 88% of its relative current density after 8000 s, implying a very good stability of this sample in HER. Meanwhile, sample 20WZ-1000 shows a good durability in OER and can retain 84% of its relative current density after 8000 s, which is higher than our previous reported core-shell based  $Co_xS_y/C$  sample produced under the same carbonization temperature that retains 80% of current density,[33] further underlining the importance role of the introduce of  $WS_2$  species in the composites. These observed good durability for the studied electrocatalysts are largely due to the stabilizing effect of porous carbon matrix on the metal sulfide catalysts, which can also provide a conducting network and electrochemical coupling between the metal sulfide active sites and the reacting species.

Since 20WZ-800 gives the best HER performance and 20WZ-1000 shows the highest OER performances among studied composites, it is interesting to find out the influence of W content on the electrocatalytic activities. In this regard, two other samples with different amount of PTA were synthesized and denoted as W10@Z67 and W30@Z67 respectively, which were used as precursors to carbonize and sulfurize at high temperatures to obtain the electrochemical evaluation samples derived at 800 °C for HER and 1000 °C for OER. Fig. 1B presents the XRD patterns of these samples obtained at 800 °C. All the three samples show diffraction peaks corresponding to metal sulfides. 30WZ-800 reveals sharper WS<sub>2</sub> peaks due to its much higher W content, vice versa for 10WZ-800.

The HER and OER polarization curves of the WZ-67 and ZIF-67 derived composites, curves for benchmark Pt/C and IrO<sub>2</sub> catalysts were also plotted for comparison. In SI Fig. S13A, although all the composites are inferior to the benchmark Pt/C in HER, 20WZ-800 shows the best performance among them. On the other hand, in SI Fig. S13B, all the composites except 30WZ-1000 outperform the benchmark IrO<sub>2</sub> in OER, and the 20WZ-1000 shows the best performance towards OER among the studied samples. Therefore, in both cases of HER and OER, the samples derived from W20@Z67 exhibits the best electrochemical performance. As has been discussed above, the generated strong electron transfer between Co and W via the intermediate Sulphur atoms, i.e. the formation of Co-W-S phase between Co<sub>1-x</sub>S-WS<sub>2</sub> interfaces could play a role in the electrochemical performance, therefore the contents of Co and W will affect the electron transfer between Co and W. While W10@Z67 (0.371g of PTA) may provide too little W and 30W@Z67 (1.113g of PTA) contains too much W, but the W20@Z67 (0.557g of PTA) leads to the appropriate amount of W required for the formation of Co<sub>1-x</sub>S-WS<sub>2</sub> phase, so as to give the best electrochemical performances in both HER and OER.

## 4. Conclusions

In summary, using the in-situ synthesized PTA@Z67 as precursor, a facile one-step carbonization and sulfurization route has been successfully developed to generate tungsten/cobalt sulfide-based carbon nanocomposite as efficient bifunctional electrocatalysts. Through the immobilization of POM molecular clusters within the confined space of ZIF-67 cages followed by heat treatment at high temperatures under H<sub>2</sub>S atmosphere, a homogeneous dispersion of tungsten sulfide and cobalt sulfide particles within a carbon matrix can be achieved. The resulting bimetallic Co-W sulfide/heteroatom doped porous carbon composites exhibit a prominent improvement in HER with Tafel slop of 64 mV/dec and an overpotential of -0.250 V (vs. RHE) at current density of 10 mA cm<sup>-2</sup>. Moreover, the bimetallic Co-W sulfide/porous carbon composites also demonstrated excellent OER activities with Tafel slop of 53 mV/dec and an overpotential of 0.365 V (vs. RHE) at current density of 10 mA cm<sup>-2</sup>, out-performing the benchmark IrO<sub>2</sub> catalyst. This work offers a new strategy to prepare homogeneous transition metal sulfide decorated porous carbon nanostructures and open up a new way to obtain a low-cost bifunctional electrocatalysts towards both OER and HER.

## Acknowledgements

The financial support by EPSRC Doctoral Training Partnership at University of Exeter and EU RFCS (RFCS-2016-754077) is greatly acknowledged.

## References

- [1] N.S. Lewis, D.G. Nocera, Powering the planet: chemical challenges in solar energy utilization, Proc. Natl. Acad. Sci. USA 103 (2006) 15729-15735.
- [2] J.A. Turner, Sustainable hydrogen production, Science 305 (2004) 972-974.

- [3] M. Gao, Y. Xu, J. Jiang, S. Yu, Nanostructured metal chalcogenides: synthesis, modification, and applications in energy conversion and storage devices, *Chem. Soc. Rev.* 42 (2013) 2986-3017.
- [4] X. Chia, A.Y. Eng, A. Ambrosi, S.M. Tan, M. Pumera, Electrochemistry of nanostructured layered transition-metal dichalcogenides, *Chem. Rev.* 115 (2015) 11941-11966.
- [5] D. Voiry, H. Yamaguchi, J. Li, R. Silva, D.C. Alves, T. Fujita, M. Chen, T. Asefa, V.B. Shenoy, G. Eda, M. Chhowalla, Enhanced catalytic activity in strained chemically exfoliated WS<sub>2</sub> nanosheets for hydrogen evolution, *Nature Mater.* 12 (2013) 850-855.
- [6] G. Ye, Y. Gong, J. Lin, B. Li, Y. He, S.T. Pantelides, W. Zhou, R. Vajtai, P.M. Ajayan, Defects engineered monolayer MoS<sub>2</sub> for improved hydrogen evolution reaction, *Nano Lett.* 16 (2016) 1097-1103.
- [7] S. Peng, L. Li, J. Zhang, T.L. Tan, T. Zhang, D. Ji, X. Han, F. Cheng, S. Ramakrishna, Engineering Co<sub>9</sub>S<sub>8</sub>/WS<sub>2</sub> array films as bifunctional electrocatalysts for efficient water splitting, *J. Mater. Chem. A* 5 (2017) 23361-23368.
- [8] L. Tao, X. Duan, C. Wang, X. Duan, S. Wang, Plasma-engineered MoS<sub>2</sub> thin-film as an efficient electrocatalyst for hydrogen evolution reaction, *Chem. Commun.* 51 (2015) 7470-7473.
- [9] G.B. de-Mello, L. Smith, S.J. Rowley-Neale, J. Gruber, S.J. Hutton, C.E. Banks, Surfactant-exfoliated 2D molybdenum disulphide (2D-MoS<sub>2</sub>): the role of surfactant upon the hydrogen evolution reaction, *RSC Adv.* 7 (2017) 36208-36213.
- [10] D. Voiry, M. Salehi, R. Silva, T. Fujita, M. Chen, T. Asefa, V.B. Shenoy, G. Eda, M. Chhowalla, Conducting MoS<sub>2</sub> nanosheets as catalysts for hydrogen evolution reaction, *Nano Lett.* 13 (2013) 6222-6227.

- [11] X. Li, G. Zhu, Q. Kang, Z.-D. Huang, X. Feng, Y. Li, R. Liu, Y. Ma, Towards free-standing MoS<sub>2</sub> nanosheet electrocatalysts supported and enhanced by N-doped CNT–graphene foam for hydrogen evolution reaction, *RSC Adv.* 5 (2015) 55396-55400.
- [12] P. Ganesan, M. Prabu, J. Sanetuntikul, S. Shanmugam, Cobalt sulfide nanoparticles grown on nitrogen and sulfur codoped graphene oxide: An efficient electrocatalyst for oxygen reduction and evolution reactions, *ACS Catal.* 5 (2015) 3625-3637.
- [13] X. Shang, J.-Q. Chi, S.-S. Lu, B. Dong, X. Li, Y.-R. Liu, K.-L. Yan, W.-K. Gao, Y.-M. Chai, C.-G. Liu, Novel Co<sub>x</sub>S<sub>y</sub>/WS<sub>2</sub> nanosheets supported on carbon cloth as efficient electrocatalyst for hydrogen evolution reaction, *Int. J. Hydrogen Energy* 42 (2017) 4165-4173.
- [14] Y.R. Liu, W.H. Hu, X. Li, B. Dong, X. Shang, G.Q. Han, Y.M. Chai, Y.Q. Liu, C.G. Liu, Facile one-pot synthesis of CoS<sub>2</sub>-MoS<sub>2</sub>/CNTs as efficient electrocatalyst for hydrogen evolution reaction, *Appl. Surf. Sci.* 384 (2016) 51-57.
- [15] X. Zhou, X. Yang, H. Li, M.N. Hedhili, K.-W. Huang, L.-J. Li, W. Zhang, Symmetric synergy of hybrid CoS<sub>2</sub>–WS<sub>2</sub> electrocatalysts for the hydrogen evolution reaction, *J. Mater. Chem. A* 5 (2017) 15552-15558.
- [16] Z. Li, L. Yin, Sandwich-like reduced graphene oxide wrapped MOF-derived ZnCo<sub>2</sub>O<sub>4</sub>–ZnO–C on nickel foam as anodes for high performance lithium ion batteries, *J. Mater. Chem. A* 3 (2015) 21569-21577.
- [17] B. Joshi, E. Samuel, Y. Il Kim, M.-W. Kim, H.S. Jo, M.T. Swihart, W.Y. Yoon, S.S. Yoon, Hierarchically designed ZIF-8-derived Ni@ZnO/carbon nanofiber freestanding composite for stable Li storage, *Chem. Engin. J.* 351 (2018) 127-134.

- [18] J.V. Morabito, L.-Y. Chou, Z. Li, C.M. Manna, C.A. Petroff, R.J. Kyada, J.M. Palomba, J.A. Byers, C.-K. Tsung, Molecular encapsulation beyond the aperture size limit through dissociative linker exchange in metal–organic framework crystals, *J. Am. Chem. Soc.* 136 (2014) 12540-12543.
- [19] H.N. Abdelhamid, Z. Huang, A.M. El-Zohry, H. Zheng, X. Zou, A Fast and scalable approach for synthesis of hierarchical porous zeolitic imidazolate frameworks and one-pot encapsulation of target molecules, *Inorg. Chem.* 56 (2017) 9139-9146.
- [20] L. Dou, S. Wu, D.-L. Chen, S. He, F.-F. Wang, W. Zhu, Structures and electronic properties of Au clusters encapsulated ZIF-8 and ZIF-90, *J. Phys. Chem. C* 122 (2018) 8901-8909.
- [21] E.L. First, C.A. Floudas, MOFomics: computational pore characterization of metal-organic frameworks, *Microporous Mesoporous Mater.* 165 (2013) 32-39.
- [22] J.J. Walsh, A.M. Bond, R.J. Forster, T.E. Keyes, Hybrid polyoxometalate materials for photo(electro-) chemical applications, *Coord. Chem. Rev.* 306 (2016) 217-234.
- [23] D.Y. Du, J.S. Qin, S.L. Li, Z.M. Su, Y.Q. Lan, Recent advances in porous polyoxometalate-based metal-organic framework materials, *Chem. Soc. Rev.* 43 (2014) 4615-4632.
- [24] J.S. Qin, D.Y. Du, W. Guan, X.J. Bo, Y.F. Li, L.P. Guo, Z.M. Su, Y.Y. Wang, Y.Q. Lan, H.C. Zhou, Ultrastable polymolybdate-based metal organic frameworks as highly active electrocatalysts for hydrogen generation from water, *J. Am. Chem. Soc.* 137 (2015) 7169-7177.
- [25] H.B. Wu, B.Y. Xia, L. Yu, X.Y. Yu, X.W. Lou, Porous molybdenum carbide nano-octahedrons synthesized via confined carburization in metal-organic frameworks for efficient hydrogen production, *Nature Commun.* 6 (2015).

- [26] Y.J. Tang, M.R. Gao, C.H. Liu, S.L. Li, H.L. Jiang, Y.Q. Lan, M. Han, S.H. Yu, Porous molybdenum-based hybrid catalysts for highly efficient hydrogen evolution, *Angew. Chem. Int. Ed.* 54 (2015) 12928-12932.
- [27] Q. Lan, Z.M. Zhang, C. Qin, X.L. Wang, Y.G. Li, H.Q. Tan, E.B. Wang, Highly dispersed polyoxometalate-doped porous  $\text{Co}_3\text{O}_4$  water oxidation photocatalysts derived from POM@MOF crystalline materials, *Chem. Eur. J.* 22 (2016) 15513-15520.
- [28] J.S. Li, Y.J. Tang, C.H. Liu, S.L. Li, R.H. Li, L.Z. Dong, Z.H. Dai, J.C. Bao, Y.Q. Lan, Polyoxometalate-based metal-organic framework-derived hybrid electrocatalysts for highly efficient hydrogen evolution reaction, *J. Mater. Chem. A* 4 (2016) 1202-1207.
- [29] Z.P. Shi, Y.X. Wang, H.L. Lin, H.B. Zhang, M.K. Shen, S.H. Xie, Y.H. Zhang, Q.S. Gao, Y. Tang, Porous nano MoC@graphite shell derived from a MOFs-directed strategy: an efficient electrocatalyst for the hydrogen evolution reaction, *J. Mater. Chem. A* 4 (2016) 6006-6013.
- [30] L. Zhang, T. Mi, M.A. Ziaee, L. Liang, R. Wang, Hollow POM@MOF hybrid-derived porous  $\text{Co}_3\text{O}_4/\text{CoMoO}_4$  nanocages for enhanced electrocatalytic water oxidation, *J. Mater. Chem. A* 6 (2018) 1639-1647.
- [31] J. Qian, F. Sun, L. Qin, Hydrothermal synthesis of zeolitic imidazolate framework-67 (ZIF-67) nanocrystals, *Mater. Lett.*, 82 (2012) 220-223.
- [32] F. Xu, T.P. Almeida, H. Chang, Y. Xia, M.L. Wears, Y. Zhu, Multi-walled carbon/IF- $\text{WS}_2$  nanoparticles with improved thermal properties, *Nanoscale*, 5 (2013) 10504-10510.
- [33] B. Chen, R. Li, G. Ma, X. Gou, Y. Zhu, Y. Xia, Cobalt sulfide/N,S codoped porous carbon core-shell nanocomposites as superior bifunctional electrocatalysts for oxygen reduction and evolution reactions, *Nanoscale* 7 (2015) 20674-20684.

- [34] Y. Feldman, E. Wasserman, D.J. Srolovitz, R. Tenne, High-rate, gas-Phase growth of MoS<sub>2</sub> nested inorganic fullerenes and nanotubes, *Science* 267 (1995) 222-225.
- [35] H. Yang, S. Liu, J. Li, M. Li, G. Peng, G. Zou, Synthesis of inorganic fullerene-like WS<sub>2</sub> nanoparticles and their lubricating performance, *Nanotechnology* 17 (2006) 1512.
- [36] M. Domínguez, E. Taboada, H. Idriss, E. Molins, J. Llorca, Fast and efficient hydrogen generation catalyzed by cobalt talc nanolayers dispersed in silica aerogel, *J. Mater. Chem.* 20 (2010) 4875-4883.
- [37] X. Li, C. Zeng, J. Jiang, L. Ai, Magnetic cobalt nanoparticles embedded in hierarchically porous nitrogen-doped carbon frameworks for highly efficient and well-recyclable catalysis, *J. Mater. Chem. A* 4 (2016) 7476-7482.
- [38] P.D. Tran, S.Y. Chiam, P.P. Boix, Y. Ren, S.S. Pramana, J. Fize, V. Artero, J. Barber, Novel cobalt/nickel–tungsten-sulfide catalysts for electrocatalytic hydrogen generation from water, *Energy Environ. Sci.* 6 (2013) 2452-2459.
- [39] J.R. Regalbuto, T.H. Fleisch, E.E. Wolf, An integrated study of Pt/WO<sub>3</sub>/SiO<sub>2</sub> catalysts for the NO • CO reaction: I. Catalyst characterization by XRD, chemisorption, and XPS, *J. Catal.* 107 (1987) 114-128.
- [40] K. Nishiyama, R. Matsuo, J. Sasano, S. Yokoyama, M. Izaki, Solid state tungsten oxide hydrate/tin oxide hydrate electrochromic device prepared by electrochemical reactions, *AIP Adv.* 7 (2017) 035004.
- [41] C. Liu, Y. Qiu, Y. Xia, F. Wang, X. Liu, X. Sun, Q. Liang, Z. Chen, Noble-metal-free tungsten oxide/carbon (WO<sub>x</sub>/C) hybrid nanowires for highly efficient hydrogen evolution, *Nanotechnology* 28 (2017) 445403.

- [42] T.A.J. Loh, D.H.C. Chua, A.T.S. Wee, One-step synthesis of few-layer WS<sub>2</sub> by pulsed laser deposition, *Sci. Rep.* 5 (2015) 18116.
- [43] J. Huang, X. Wang, J. Li, L. Cao, Z. Xu, H. Wei, WS<sub>2</sub>-Super P nanocomposites anode material with enhanced cycling stability for lithium ion batteries, *J. Alloys Compd.* (2016) 60-66.
- [44] J. Wang, R. Ma, Z. Zhou, G. Liu, Q. Liu, Magnesiothermic synthesis of sulfur-doped graphene as an efficient metal-free electrocatalyst for oxygen reduction, *Sci. Rep.* 5 (2015) 9304.
- [45] G. Li, J. Sun, W. Hou, S. Jiang, Y. Huang, J. Geng, Three-dimensional porous carbon composites containing high sulfur nanoparticle content for high-performance lithium-sulfur batteries, *Nature Commun.* 7 (2016) 10601.
- [46] A. Dychalska, P. Popielarski, W. Frankow, K. Fabisiak, K. Paprocki, M. Szybowicz, Study of CVD diamond layers with amorphous carbon admixture by Raman scattering spectroscopy, *Mater. Sci.* 33 (2015) 799-805.
- [47] H. Jiang, J.X. Gu, X.S. Zheng, M. Liu, X.Q. Qiu, L.B. Wang, W.Z. Li, Z.F. Chen, X.B. Ji, J. Li, Defect-rich and ultrathin N doped carbon nanosheets as advanced trifunctional metal-free electrocatalysts for the ORR, OER and HER, *Energy Environ. Sci.* 12 (2019) 322-333.
- [48] J.D. Benck, T.R. Hellstern, J. Kibsgaard, P. Chakthranont, T.F. Jaramillo, Catalyzing the hydrogen evolution reaction (HER) with molybdenum sulfide nanomaterials, *ACS Catal.* 4 (2014) 3957-3971.
- [49] Y.H. Li, P.F. Liu, L.F. Pan, H.F. Wang, Z.Z. Yang, L.R. Zheng, P. Hu, H.J. Zhao, L. Gu, H.G. Yang, Local atomic structure modulations activate metal oxide as electrocatalyst for hydrogen evolution in acidic water, *Nature Commun.* 6 (2015) 8064.

- [50] T. Zheng, W. Sang, Z. He, Q. Wei, B. Chen, H. Li, C. Cao, R. Huang, X. Yan, B. Pan, S. Zhou, J. Zeng, Conductive tungsten oxide nanosheets for highly efficient hydrogen evolution, *Nano Lett.* 17 (2017) 7968-7973.
- [51] M. Jahan, Z. Liu, K.P. Loh, A graphene oxide and copper-centered metal organic framework composite as a tri-functional catalyst for HER, OER, and ORR, *Adv. Funct. Mater.* 23 (2013) 5363-5372.
- [52] L. Wang, X. Wu, S. Guo, M. Han, Y. Zhou, Y. Sun, H. Huang, Y. Liu, Z. Kang, Mesoporous nitrogen, sulfur co-doped carbon dots/CoS hybrid as an efficient electrocatalyst for hydrogen evolution, *J. Mater. Chem. A* 5 (2017) 2717-2723.
- [53] Y. Jia, L.Z. Zhang, A.J. Du, G.P. Gao, J. Chen, X.C. Yan, C.L. Brown, X.D. Yao, Defect graphene as a trifunctional catalyst for electrochemical reactions, *Adv. Mater.* 28 (2016) 9532-9538.
- [54] L. Wu, K. Zhang, T. Wang, X. Xu, Y. Zhao, Y. Sun, W. Zhong, Y. Du, Cobalt sulfide nanotubes ( $\text{Co}_9\text{S}_8$ ) decorated with amorphous  $\text{MoS}_x$  as highly efficient hydrogen evolution electrocatalyst, *ACS Appl. Nano Mater.* 1 (2018) 1083-1093.